Competing anisotropies in exchange-biased nanostructured thin films

F. J. T. Goncalves,* G. W. Paterson, and R. L. Stamps
SUPA, School of Physics and Astronomy, University of Glasgow, Glasgow G12 8QQ, United Kingdom

S. O'Reilly and R. Bowman
ANSIN, Department of Physics and Astronomy, Queen's University Belfast, Belfast BT7 1NN, United Kingdom

G. Gubbiotti
Instituto Officina dei Materiali del Consiglio Nazionale delle Ricerche (IOM-CNR), Sede Secondaria di Perugia, c/o Dipartimento di Fisica e Geologia, Via A. Pascoli, I-06123 Perugia, Italy

D. S. Schmool
Groupe d'Etude de la Matière Condensée GEMaC, CNRS (UMR 8635), Université de Versailles/Saint-Quentin-en-Yvelines, 45 Avenue des États-Unis, 78035 Versailles, France

(Received 16 April 2016; revised manuscript received 5 July 2016; published 15 August 2016)

The magnetic anisotropies of a patterned, exchange biased $Fe_{50}Mn_{50}/Ni_{80}Fe_{20}$ system are studied using ferromagnetic resonance, supplemented by Brillouin light scattering experiments and Kerr magnetometry. The exchange biased bilayer is partially etched into an antidot geometry so that the system approximates a $Ni_{80}Fe_{20}$ layer in contact with antidot structured $Fe_{50}Mn_{50}$. Brillouin light scattering measurements of the spin wave frequency dependence on the wave vector reveal a magnonic band gap as expected for a periodic modulation of the magnetic properties. Analysis of the ferromagnetic resonance spectra reveals eightfold and fourfold contributions to the magnetic anisotropy. Additionally, the antidot patterning decreases the magnitude of the exchange bias and modifies strongly its angular dependence. Softening of all resonance modes is most pronounced for the applied magnetic field aligned within 10° of the antidot axis, in the direction of the bias. Given the degree to which one can tailor the ground state, the resulting asymmetry at low frequencies could make this an interesting candidate for applications such as selective/directional microwave filtering and multistate magnetic logic.

DOI: 10.1103/PhysRevB.94.054417

I. INTRODUCTION

Periodically patterned holes in a magnetic film can be used to affect microwave-frequency response, and are used in magnonic devices, spin wave logic [1,2], interferometry, and filtering devices [3]. An interesting aspect of patterned films is that they induce a nonuniform magnetization reversal process, which can be advantageous for the development of multistate memory devices [4–6]. A stepped magnetization reversal, necessary for such applications, can be achieved by patterning a bicomponent structure, typically comprised of antidot structuring with the holes filled with a different magnetic material [7–10], or by adding positive or negative exchange bias on a single ferromagnetic layer system [4,11]. Exchange bias can also be seen as a way to modify the dynamic response of the magnetic system, as a result of the competing unidirectional and anisotropic field distribution [12]. In particular, an asymmetric microwave response with respect to the applied field has been demonstrated to originate in the unbalanced pole distribution at the edges of the holes in the antidot lattice (ADL) [13].

We report the magneto-dynamic properties of an antiferromagnet-ferromagnet system with antidot structuring on the antiferromagnet, but incomplete holes in the ferromagnetic layer, studied using ferromagnetic resonance (FMR) and Brillouin light scattering (BLS). This type of structuring results in a periodic modulation of the ferromagnetic layer thickness and exchange bias between the holes. The layer configuration is illustrated in Fig. 1(a). Having a continuous film adjacent to the ADL allows the spin wave modes to have a complex dependence on the applied field angle, as spin waves can potentially be allowed to propagate in all directions [7]. The concept of partially etched ADL has been reported in Ref. [14], where the two resonance modes observed both via all-electric spin wave spectroscopy and micro-focused BLS on an ADL with 1-μm pitch and 435-nm hole diameter, have been attributed to the hole and interhole channels, which are perpendicular to the applied magnetic field direction. The sample reported here is different in terms of the lattice parameters, etch depth and presence of the exchange bias field. Applied magnetic field angle-dependent FMR results show a combined eightfold and fourfold symmetry for the lowest-frequency resonance modes and a dominant fourfold symmetry for the highest-frequency resonances. Also, the variation of the exchange bias field with applied field direction exhibits an interesting dependence. It is widely known that exchange bias in continuous films possesses a unidirectional symmetry with regards to an external field [15,16]. However, in the case of the ADL here studied, the effect of exchange bias on the FMR properties appears to vary greatly with the angle between the external magnetic field and the symmetry of the ADL structuring. Previous reports focused mainly on the effect of ADL on the net exchange bias field [4,11,17,18], which in turn was observed to affect the static magnetization, without providing detail on the angular dependence of the FMR

*fisica.francisco@gmail.com

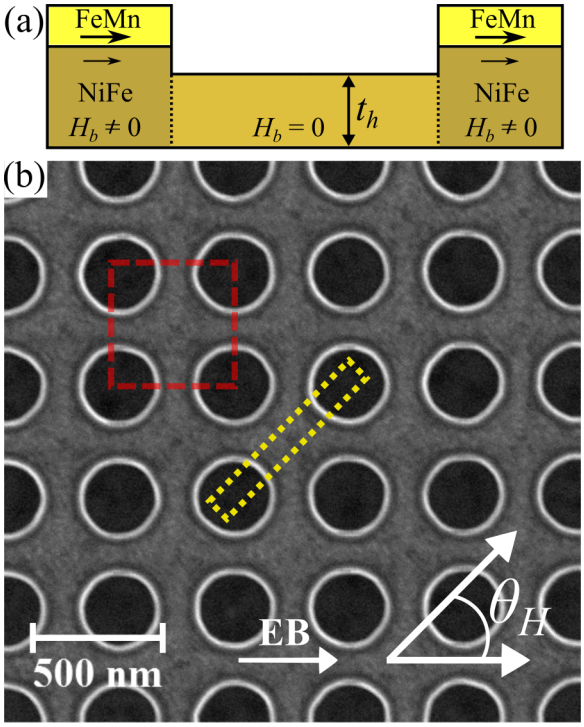

FIG. 1. (a) Schematic of the cross-section view of the partially etched ADL. The ADL consists of a fully etched FeMn layer adjacent to a partially etched NiFe layer. The thickness of the remaining NiFe is labeled as t_h. A nonzero exchange bias field, H_b, is expected right underneath the FeMn layer while in the regions from which the FeMn has been removed the expected value for H_b is zero. (b) SEM image of the NiFe(20 nm)/FeMn(10 nm) ADL fabricated. The red dashed square illustrates the ADL unitary cell whose side is 420 nm long. The hole diameter is 280 nm. The yellow dashed rectangle illustrates the orientation of the cross-section used in the morphology and elemental analysis presented in Fig. 2.

modes we address in this manuscript. Using micromagnetic modeling, we obtain simulated resonance spectra, which is in good agreement with the experimental FMR and BLS data. The resonance spectra as a function of the applied field angle and the spatial distribution of the precessional modes were investigated in order to determine the origin of the eightfold anisotropy observed in the experiments. Modes are considered to be localized when the precession amplitude is confined to the edges of the holes and extended when the maximum precession amplitude extends across the ADL. This nomenclature has been introduced in Refs. [19,20] and since then used in several Refs. [21–24]. Here, it is found that an eightfold anisotropy emerges due to the partial patterning in the FM layer, causing an overlap in resonance frequency between the localized (or edge) mode and the first extended mode. Importantly, despite being partially patterned across the whole thickness, the structure behaves as magnonic crystal exhibiting characteristic spin wave band gaps induced by the artificial periodicity of the ADL.

The manuscript is structured as follows: the details of the film growth, patterning, structural analysis and magnetometry data are presented in Sec. II. The magnetodynamic properties of the patterned films studied by FMR and BLS, and the effect of patterning on the magnetic anisotropies are discussed in Sec. III. In Sec. IV, we present and discuss the micromagnetic simulations carried out to interpret the origin of the anisotropy in this particular ADL system.

II. FILM GROWTH AND PATTERNING

A Si substrate was sputtered with an 8-nm-thick layer of tantalum (Ta), acting as a buffer layer, and followed by the sequential deposition of $Fe_{20}Ni_{80}$ and $Fe_{50}Mn_{50}$ in a sputtering system (Shamrock SFI) at a base pressure of 10^{-8} mbar in the presence of an in-plane magnetic field of 9 mT. The bilayer was capped with an 8-nm Ta layer to prevent oxidization. Following deposition, the sample was annealed at 498 K in a 0.2 T magnetic field (3 °C/minute ramp, 120 minutes at maximum temperature) in order to set the exchange bias direction. To initiate the patterning process, a 220 nm thick layer of silicon nitride (SiN) was deposited on top of the Ta layer, with the purpose of using it as a hard mask. The sample was subsequently patterned using electron beam lithography combined with reactive ion etching. The whole process was carried out in three main steps: (1) a 200-nm-thick layer of ZEP520 resist was deposited on top of the SiN, subsequently exposed on a Vistec VB6 UHR EWF e-beam writer and developed in O-Xylene; (2) the developed pattern was transferred to the hard mask via a reactive ion etching process (RIE) using CHF_3/O_2 in a 80+RIE etching tool; (3) the NiFe/FeMn/Ta was etched on a ET340 RIE tool using CH_4/H_2 [25]. The estimated etching rate for the NiFe/FeMn/Ta layers was 3 nm/min. The ADL covered an area of $1.5 \times 1.5\,mm^2$. The unit cell size is 420 nm, with 280-nm diameter holes. A scanning electron microscopy (SEM) image of the structure is shown in Fig. 1(b).

An area of the substrate ($5 \times 5\,mm^2$) which was subject to the fabrication process but remained unpatterned was used as a reference in the study of the magnetic properties of the continuous films. In Appendix A, we compared the resonance properties of this continuous film with those of the continuous film as-deposited. The results suggest that the fabrication process did not affect the exchange bias properties of the continuous film.

Conventional transmission electron microscopy and electron energy loss spectroscopy (EELS) studies on a cross section of the sample were performed in order to determine the thickness and the elemental composition of each layer. EELS measurements were performed in a probe corrected JEOL ARM200F scanning transmission electron microscope operated at 200 keV and equipped with a cold field emission electron gun and a GIF Gatan Quantum ER spectrometer. The EELS data were collected at a dispersion of 1.2 meV/channel (5 eV / 4096 channels) and pixel size of 1.54 nm. Figures 2(a)–2(c) show a cross-section of the ADL which was prepared by focused ion beam (FIB) with a cut along the lattice diagonal. We note a that the unetched sections of the ADL are protected by a trapezoid shaped section of SiN. This shape is a result of the etch rates for the different elements during the RIE process. In Fig. 2(b), the regions labeled as I and II refer to the Ta/NiFe and the Ta/NiFe/FeMn/Ta, respectively. The elemental maps of each region are shown in Fig. 2(d). From analyzing region I, the presence of Si, Ta, Ni, Fe, C, O,

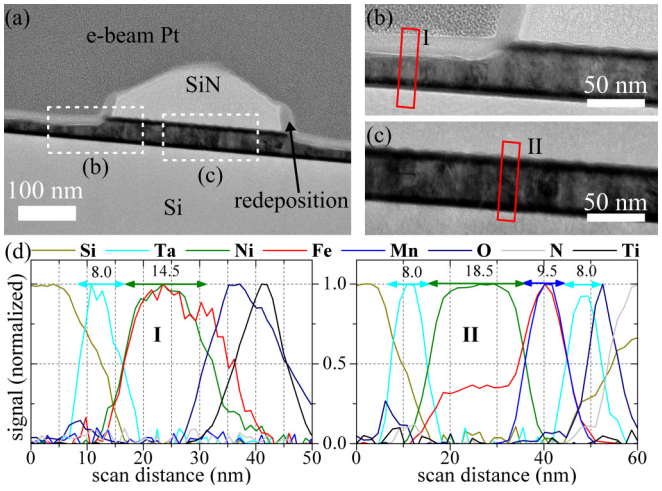

FIG. 2. (a)–(c) Bright field TEM images of the ADL cross-section. (d) EELS data relative to the region I and region II. Elemental profiles (normalized signal) of the regions I and II indicated in (b) and (c), with the layer thickness shown for each of the relevant layers. The dashed yellow rectangle shown in Fig. 1(b) illustrates the orientation of the cross-section with regards to the ADL. Redeposition of material may have occurred during the etching process. The e-beam Pt at the top was deposited to protect the specimen during the FIB cut.

Pt, and Ti were detected, from the substrate to the top of the film. Although it has not been possible to identify the origin of the Ti, it is believed that its origin is related to contamination during the etching process since this element only appears in regions exposed to the reactive ion etching process. The presence of C and O are the result of etching and the fact that this surface, rich in Ni and Fe, was not capped in any way, promoting the formation of oxides at the interface as well as a carbon layer. In region II, one is able to identify the elements Si, Ta, Ni, Fe, Mn, Ta, and N. Based on the elemental composition shown in Fig. 2(c) relative to the several elements across the sample, the thickness is estimated for the case of the Ta, NiFe and FeMn layers. This is done by measuring the width at half height of the elemental distribution.

Magneto-optic Kerr effect (MOKE) magnetometry was employed to study the hysteretic behavior of the continuous (a) and the patterned ADL (b) films. MOKE hysteresis loops are shown in Fig. 3 for both the (a) continuous NiFe/FeMn films and (b) ADL. The setup was operated in the longitudinal configuration, with a laser spot size of 500 μm in diameter. For the continuous film, the hysteresis was obtained while the external magnetic field was applied parallel ($\theta_H = 0°$) and perpendicular ($\theta_H = 90°$) to the exchange bias direction and the ADL axis [Fig. 1(b)]. The results show a clear easy axis direction with an exchange bias field magnitude $H_b \sim 5$ mT. In the case of the ADL, the hysteresis was measured with the external field applied along the lattice edges. For both $\theta = 0°$ and 90°, the exchange bias field magnitude $|H_b| = 1.5$ mT. In a patterned film, the low-field magnetization processes are dominated by the ADL anisotropy so the effect of exchange bias is not as trivial as a lateral shift in the hysteresis loop commonly observed in continuous exchange bias films. The fact that both directions exhibit a net exchange bias field

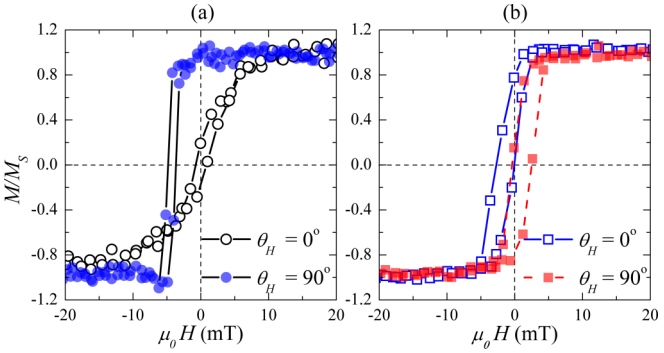

FIG. 3. Hysteresis loops obtained from MOKE measurements of (a) the continuous film while the external field was applied parallel ($\theta_H = 0°$) and perpendicular ($\theta_H = 90°$) to the exchange bias direction; and (b) the ADL while the external field is applied along the edges of the ADL, which coincide with the directions $\theta_H = 0°$ and 90°.

suggests that a transformation of the exchange bias symmetry has occurred due to the ADL patterning. This aspect will be discussed when looking at the ferromagnetic resonance results.

III. MODE STRUCTURE

Broadband ferromagnetic resonance spectroscopy was performed using a vector network analyser (Rohde & Schwarz ZVA40), VNA-FMR. The sample was placed on top of a coplanar waveguide with the system operating in a two-port configuration. Each measurement was initiated well above the saturation field, at $\mu_0 H = 150$ mT, where a reference spectrum was acquired for background correction. Then, starting at a maximum applied field $\mu_0 H = 65$ mT, the VNA frequency was swept and the averaged (5 times) forward scattering parameter, S_{21} recorded. The static external magnetic field was linearly reduced once the frequency sweep was completed. This procedure was repeated in the applied field range of $|\mu_0 H| \leqslant 65$ mT in field steps of 1.2 mT. As a final outcome, we obtained the relative variation of the magnitude of the parameter S_{21} as a function of the microwave frequency and external magnetic field.

Brillouin light scattering (BLS) is an optical technique that relies upon the inelastic scattering of light from spin wave excitations in magnetic systems, enabling the study of wave vector resolved spin wave dispersion [26]. The principle consists of the interaction of photons with a certain energy and momentum $(\hbar\omega_I, \hbar\vec{k}_I)$ with magnons $(\hbar\omega, \hbar\vec{k})$. The terms ω and $\vec{k}$ correspond to the frequency and wave vector of the incident photons and magnons. The annihilation or creation of optically excited magnons can be retrieved by measuring the energy and momentum transfer of the scattered photons $\hbar\omega_S(\vec{k}_S) = \hbar(\omega_I(\vec{k}_I) \pm \omega(\vec{k}))$. BLS experiments were performed in the backscattering configuration using a Sandercock (3+3)-type tandem Fabry-Perot interferometer. Spectra were acquired in the Damon-Eshbach (DE) scattering configuration ($\vec{k} \perp \vec{H}$). The wavelength of the incident laser light was $\lambda = 532$ nm. Due to a photon-magnon conservation of momentum in the scattering process, the in-plane component of the excitation wave vector (k) varies with the incidence angle of light (θ)

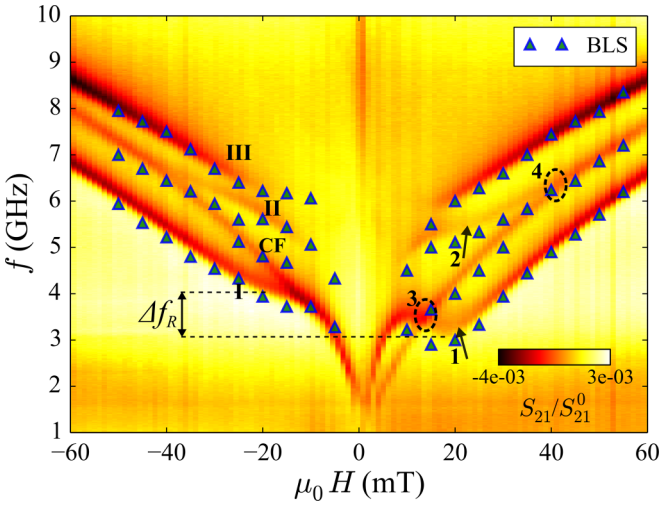

FIG. 4. Contour plot of the normalized magnitude of the forward scattering parameter S_{21}, representing the ferromagnetic resonance data of the ADL. The scatter plot (blue triangles) corresponds to the BLS data at $\theta_H \sim 0^\circ$. From lower to higher frequencies, four resonance modes are labeled as I, CF, II, and III. The field/frequency regions numbered as 1 and 2 highlight the softening of the modes I and II, respectively. The regions numbered as 3 and 4 indicate intersection of mode CF with the modes I and II, respectively. The term Δf_R represents the asymmetry in frequency of mode I between the resonance at $\mu_0 H = -20$ and 20 mT.

according to $k = (4\pi/\lambda)\sin\theta$, where λ is the light wavelength. A static external field of $\mu_0 H = 50$ mT was applied in the direction parallel to the lattice edge and collinear with the exchange bias direction, consistent with $\theta_H = 0^\circ$ of Fig. 1(b).

A. Field dependent magnetodynamics using VNA-FMR and BLS

The ferromagnetic resonance spectra shown as color plot in Fig. 4 were obtained from the ADL sample, where the magnetic field is applied parallel to the lattice edge ($\theta_H = 0^\circ$) and the exchange bias direction. The full spectra contains four resonances and all are centered at around $\mu_0 H \sim 0$ mT. The modes are labeled as I, CF, II, and III, from lower to higher frequencies. The mode CF is labeled differently since its origin is related to the continuous film underneath the ADL [recall Figs. 1(a) and 2(a)]. The modes I, II, and III are intrinsically related to the patterned layer. Features worth noting are the field regions at which softening of modes I and II occur. These are indicated with arrows numbered as 1 and 2, respectively. For the case where the applied field is aligned with the edges of the lattice, the magnetization reversal undergoes a hard-axis-like behavior, i.e., at a certain stage of the reversal, the external field cancels the effective anisotropy, allowing for local reorientation of the magnetic domains. Consequently, the resonance frequency drops to a minimum value, as a result of the vanishing torque along the applied field direction [27]. When the applied field is lower than the anisotropy field, the torque is restored and the resonance frequency increases. The regions in the spectra highlighted with dashed circles and numbered as 3 ($\mu_0 H \sim 15$ mT) and 4 ($\mu_0 H \sim 40$ mT) indicate the overlap between the resonance mode CF and modes I and II, respectively.

One should also note the effect of exchange bias in the FMR response. This appears as a lateral displacement of the spectra and a noticeable asymmetry in resonance frequency between positive and negative applied fields. The asymmetric behavior results from the unidirectional nature of the exchange bias field, which at positive applied fields shifts the resonance frequency downwards, whereas for negative fields the resonances are shifted upwards, giving rise to an asymmetry noted in the spectra by Δf_R. For the case of mode I, an asymmetry $\Delta f_R = 1$ GHz is obtained when evaluating the difference in resonance frequency at the applied field of $\mu_0 H = 20$ and -20 mT. A similar behavior is observed for resonance mode II, where the asymmetry $\Delta f_R = 0.4$ GHz for $|\mu_0 H| = 20$ mT. The asymmetry is expected to be larger when $\mu_0 H \simeq H_k$ since that, due to mode softening, the exchange bias field becomes the only ordering parameter for the magnetization. Field dependent BLS data (triangular symbols) are also shown in Fig. 4. Note the good agreement with the FMR data. The small deviations between the FMR and BLS data can originate from a possible misalignment of the sample relative to $\theta_H = 0^\circ$. The wave-vector dispersion studied using BLS is discussed in the following section.

B. Spin wave dispersion using BLS

Figure 5 shows the spin wave frequency dispersion (frequency versus wave vector) of the ADL (open circles) and the continuous exchange biased film (red squares). The largest wave number measured was $k_{\max} = 2.6 \times \pi/a$, with a being the hole spacing (420 nm), which, in the reciprocal space corresponds to a wave vector just above the second Brillouin

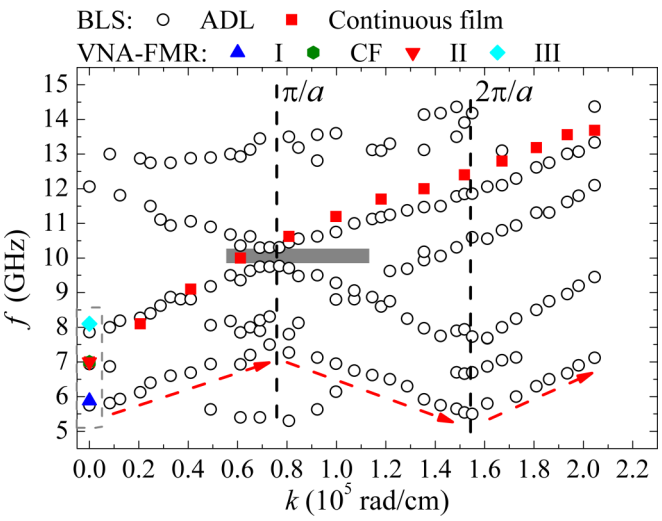

FIG. 5. BLS measurements at $\theta_H = 0^\circ$, while in the presence of an external field $\mu_0 H = 50$ mT, of the ADL (open circles) and the continuous film (red squares). For $k = 0$ the resonances match the FMR data. The periodicity of the lattice causes a change in the slope of the dispersion modes at $k = \pi/a$ and $2\pi/a$ as highlighted by the red dashed arrows. The magnonic band gap is highlighted by the grey shaded area at (π/a rad cm^{-1}, ~10 GHz). The spin wave wave vector is perpendicular to the applied field direction (DE configuration).

zone. When the light is focused at normal incidence upon the sample surface ($k = 0$), the modes agree well with the resonance peaks obtained from the VNA-FMR experiments. Similarly to the FMR results, at $k = 0$, the resonance mode CF overlaps with mode II from the ADL.

In materials with modulated magnetic properties, the spin wave dispersion relation exhibits prohibited and allowed frequency bands, similarly to the case of electron scattering due to an atomic lattice or the diffraction of photons in the case of a photonic crystal. In Fig. 5, note the existence of a forbidden band gap, 0.6-GHz wide, at $k = 0.77\times10^5$ rad cm^{-1} (π/a), located at the boundary of the first Brillouin zone (grey shaded rectangle). The emergence of a band gap is evidence of repulsive interactions due to Bragg scattering of spin wave modes. Experimental evidence for Bragg scattering of spin waves was first demonstrated in Ref. [28] for the case of simple two dimensional nanostructures. In Ref. [29], the spin wave dispersion for a type of bicomponent ADL demonstrated the emergence of a BG. Reference [30] demonstrates that having a nonmagnetic Ag ADL on top of a ferromagnetic continuous film can induce selectivity in the spin wave spectra. The results presented in the present manuscript show that the formation of band gap is also possible in the current geometry while in the presence of spatially modulated exchange bias field. The periodicity of the lattice is reflected in the BLS data, as can be seen by following the dispersion branches which have inflection points at the boundaries of the Brillouin zone. The frequency variation of these modes is highlighted by the red dashed arrows.

C. Magnetic anisotropies

In-plane angular dependent FMR measurements were performed in order to evaluate the anisotropic behavior of the resonance modes. In the angular range of $\theta_H = [0°–190°]$, FMR spectra were acquired every 10°, while around [0°,45°,90°] the step was reduced to 5°. Representative spectra are shown in Fig. 6. On all spectra the dashed lines represent the fit to each resonance mode using a Kittel-like resonance equation shown in Eq. (2).

The data corresponding to $\theta_H = 10°$ shown in Fig. 6 is used to demonstrate the existence of two softening regions (black arrows) in the field range presented. In particular, at an applied field of $\mu_0 H \simeq -15$ mT, the decrease in resonance frequency of mode I is associated with the balance between the external field and the effective anisotropy which includes the ADL anisotropy, H_k, due to patterning and the exchange bias field, H_b. The difference in resonance behavior at positive and negative applied fields is related to the exchange bias field which, for positive applied fields, counts as a positive contribution to the anisotropy, whilst for negative applied fields, counts as a negative contribution.

In the low-field regions, near $\mu_0 H \sim 0$ mT, the magnetization undergoes the reversal process, as we have also observed in the MOKE data shown in Fig 3. The reversal process is widely understood as mode softening followed by complete reversal of the magnetization via domain formation and rotation [24,31–33]. Similar resonance behavior is observed when the applied field is set along, for example, $\theta_H = 20°$ and 30°. In these spectra, the resonance frequency of mode I is higher when compared to that of $\theta_H = 0°$, and therefore the resonance in the direction between 20° and 30° behaves like an easy axis, as opposed to the directions $\theta_H = 0°$, 45°, and 90° where a hard-axis behavior is observed. It is important to note that in principle, the $\theta_H = 45°$ hard-axis anisotropy is lower than the anisotropy along the directions $\theta_H = 0°$, 90°, since the drop in the resonance frequency is less pronounced. This can be easily seen in Fig. 7, where we show a detailed analysis of the anisotropy field as a function of the applied field angle θ_H.

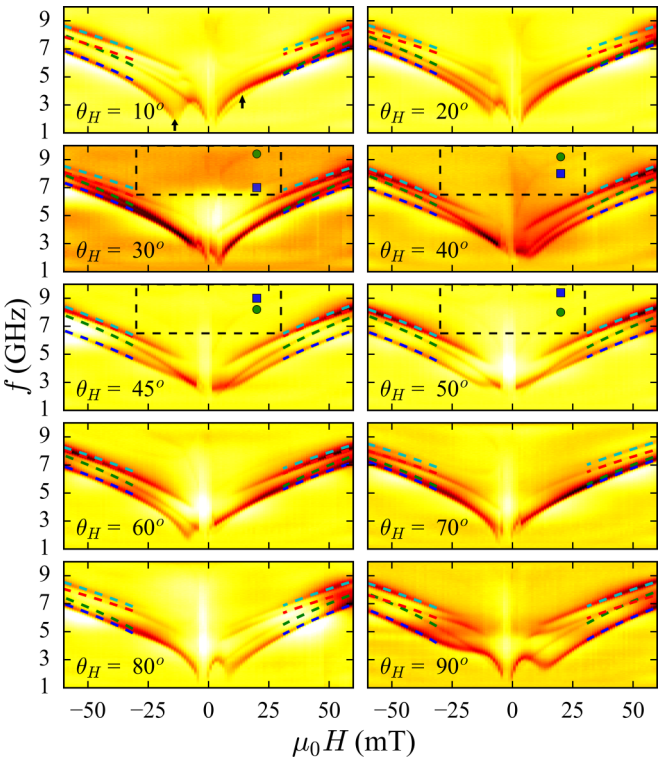

FIG. 6. Color plots of the FMR data (normalized magnitude of S_{21}) at different applied field angles, θ_H. Each resonance mode was fitted with a Kittel-like resonance equation and the results of the fitting are plotted using the dashed lines. The vertical arrows in $\theta_H = 10°$ indicate the field region where mode softening occurs. Mode softening strongly depends upon the applied field angle. The dashed rectangles in spectra corresponding to $\theta_H = [30°–50°]$ highlight high-frequency modes, which appear only at certain angles. These are also labeled with square and circular symbols in the spectra corresponding to $\theta_H = 45°$ and 50°. The low signal to noise ratio prevents a more detailed study of these modes.

A detailed description of the anisotropies of the different resonance modes is now presented and discussed. The anisotropy parameter for each mode was obtained by simultaneously fitting all the resonance modes obtained at each spectra. The multipeak fit done in the field range within 60 mT $< |\mu_0 H| >$ 35 mT, thus considering only the saturated states. In this field range, we assume that the domain textures which are inherent to low-field region are suppressed due to the presence of a relatively large applied field magnitude. The fittings were performed on the derivative of the experimental data so a derivative of the Lorentzian function was used to fit each resonance line, with an average R^2 of 0.88±0.04.

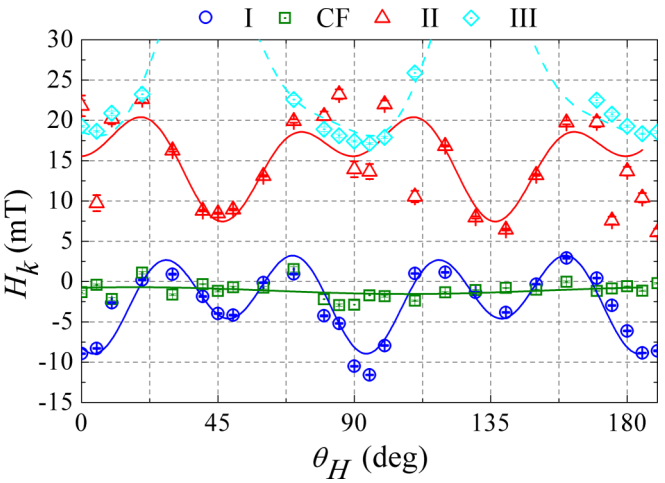

FIG. 7. Angular variation of the anisotropy fields obtained by fitting Eq. (2) to the experimental data (symbols) for modes I, CF, II, and III (error bars included with the symbols). The continuous lines represent a fit to the proposed model for the anisotropy, shown in Eq. (3). The dashed line (cyan) is in agreement with the behavior of mode III, which will be discussed later.

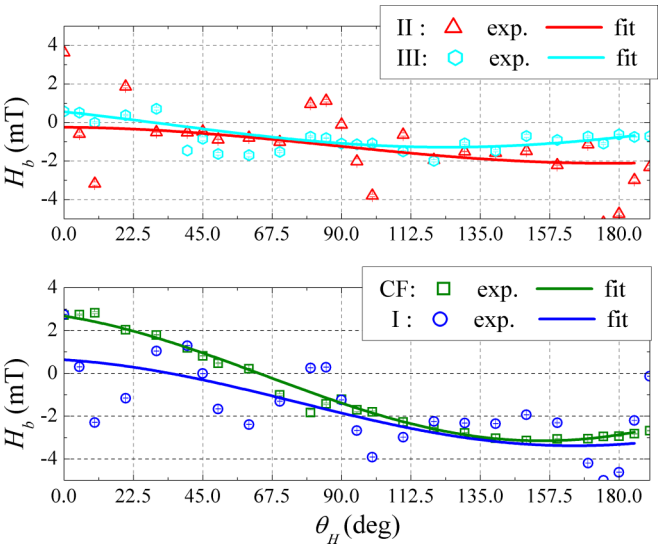

FIG. 8. Angular variation of the exchange bias field (symbols) and fits (lines) to the experimental data using Eq. (4).

An example of the fitting process is given in Appendix B. At each angle, the data was fitted with four resonance lines, as illustrated in Fig. 6 by the four dashed lines, allowing the assessment of the anisotropy field, the exchange bias field and the effective magnetization, following a generalized Kittel formula [34]:

$$f^2 = \gamma^2(|H + H_b| + H_k)(|H + H_b| + H_k + \mu_0 M), \quad (1)$$

where γ is the electron gyromagnetic ratio. Assuming that $\mu_0 M \gg |H + H_b| + H_k$, in Eq. (1) leads to the approximation

$$f^2(\theta) \approx \gamma^2(|H + H_b| + H_k)\mu_0 M_{\text{eff}}, \quad (2)$$

where M_{eff} is the effective magnetization.

The anisotropy field as function of angle, $H_k(\theta_H)$, obtained from fitting to the experimental data with Eq. (2), is plotted in Fig. 7. The results suggest the presence of an overlapping eightfold an fourfold anisotropy terms. The solid lines represent a fit to Eq. (3), which accounts for an offset constant, H_k^0, and four and eightfold anisotropy constants, which are labeled as H_k^4 and H_k^8, respectively. In particular for mode I, the eightfold and fourfold dependence can be clearly seen by following the continuous blue line. An uniaxial anisotropy constant was not used here given that both the CF mode and the continuous film (Appendix A) data exhibited a negligible anisotropy field:

$$H_k(\theta_H) = H_k^0 + H_k^4 \cos^2(2(\theta_H + \theta_0)) + H_k^8 \cos^2(4(\theta_H + \theta_0)), \quad (3)$$

$$H_b(\theta_H) = H_b^0 + H_b^1 \cos(\theta_H + \theta_0). \quad (4)$$

Figure 8 shows the angular variation of the exchange bias field, H_b, for all modes. The continuous lines are fits of Eq. (4) to the experimental data. It is important to note that the angular dependence of mode CF is in agreement with the angular variation of a continuous exchange biased film [35], as also demonstrated using micromagnetic simulations [see Fig. 15(d) of Appendix C].

The exchange bias field magnitude obtained in mode I appears to change from positive to negative amplitude when θ_H changes by 22.5°. This angular dependence illustrates an interesting property of this magnetic system whereby the combined anisotropies give rise to an apparent anisotropic dependence of the exchange bias field with regards to the applied field direction, which may be associated with modifications in the coercivity due to the ADL structuring. Alternatively, one could consider the occurrence of deformations in the spin texture at the interface between the NiFe and the FeMn films, allowing for the exchange bias to behave as a rotatable anisotropy. Having obtained a residual anisotropy for the CF mode and on the other obtained a good agreement between the Eq. (4) and the exchange bias field dependence across all field directions, we considered that effects such as rotatable anisotropy and training effects are negligible in this exchange bias system. These effects would in any case be highly suppressed due to the strong local modifications to the anisotropy imposed by the structuring. Moreover, in Sec. IV, we will demonstrate that micromagnetic simulations support our decision to exclude such artifacts. Although the mechanism for this is not fully understood, this feature could possibly enable the use of such systems as tunable microwave filtering devices.

Table I summarizes the fitting terms for the values of $H_k(\theta_H)$ and $H_b(\theta_H)$ described in Eqs. (3) and (4). A fitting parameter, θ_0, was added to account for a possible misalignment between the exchange bias axis and the edges of the ADL and experimental error in measuring the in-plane rotation angle. This small offset angle can be observed in Figs. 7 and 8 as a lateral displacement of the local extrema with regards to the main directions, $\theta_H = 0°$ and 90°.

The angular variation of modes II and III is rather complicated to follow, given the strong dependence on the anisotropy and the overlapping of the modes. However, it is noted that the angular dependence of these two modes appears to be shifted by 45° with regards to one another. Also, in the angular

TABLE I. Fitting parameters for the anisotropy, bias, and effective magnetization of the ADL. Units of the fitting parameters expressed in millitesla, with exception of M_{eff}, which is expressed in tesla. The fitting parameter θ_0 is $\sim 11^\circ$.

mode	H_b^0	H_b^1	H_k^0	H_k^4	H_k^8	M_{eff}
I	−1.6	1.8	−8.9	−4.5	8.6	1.1
CF	0.05	3.5	−1.7	−1.0	–	1.3
II	−1.7	2.4	7.4	−7.2	−7.6	1.1
III	−0.1	1.17	13.6	22.1	5.6	1.2

range of $\theta_H = [22.5^\circ$–$67.5^\circ]$, it appears that the anisotropy field of mode III increases substantially, which suggests that in the VNA-FMR data, this mode could be shifting to higher frequencies than covered in this measurement. The limited sensitivity of the VNA-FMR apparatus constrained observations at higher frequency. Thus it is only possible to make a qualitative description of these modes. In Fig. 6, at angles corresponding to the range $\theta_H = [30^\circ$–$50^\circ]$, two sets of symbols were added (square and circular shapes) to highlight two frequency modes, which appear within the frequency and field range marked with the dashed grey rectangles. To aid the discussion, the region of the spectra where these two modes appear is shown in more detail in Fig. 9. The modes in the frequency region between 7–10 GHz are labeled as IV and V and highlighted with blue and green dashed lines, respectively, so that they are more easily followed. Note that when θ_H changes from 30° to 40°, mode IV moves upwards in frequency, while mode V moves downwards. At $\theta_H = 40^\circ$, both modes intercept at $(\mu_0 H,\ f) \sim$ (14 mT, 8.2 GHz). In the spectra corresponding to $\theta_H = 45^\circ$ and 50°, modes IV and V continue their ascending and descending movements, respectively. The ascending movement of mode IV may be understood as the continuation of the mode III, as suggested by the trend of the anisotropy field discussed in Fig. 7. An alternative description is that mode III remains in the same frequency range as mode II. However, our interpretation is that mode III undergoes an increase in resonance frequency, whose movement is given by mode IV, which is consistent with the combined eightfold and fourfold anisotropy obtained from modes I and II and III. Mode V moves downwards in frequency with increasing θ_H and may be related to the resonance mode observed at 12.01 GHz in the BLS spectra (Fig. 5). The fact that these two modes change rapidly with θ_H suggests great sensitivity to the anisotropy of the patterned structure.

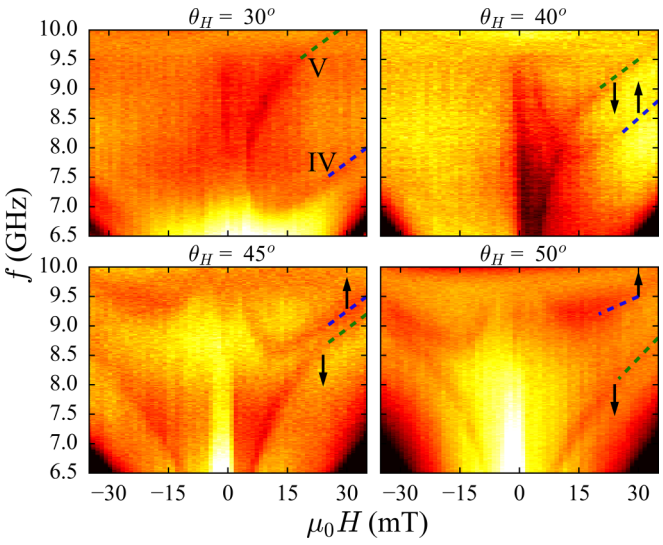

FIG. 9. Resonance modes IV and V with low FMR amplitude appear the high-frequency region. These spectra correspond to sections of the data shown in Fig. 6 but with improved contrast. The arrows indicate the direction of motion with increasing θ_H.

IV. PARTIAL PATTERNING AND MODE ANALYSIS

Following the cross-sectional studies of Fig. 2, the NiFe remaining in the holes is approximately 14.5 nm in thickness and therefore it is expected to play a significant role in defining the FMR properties. With this in mind, a comparative micromagnetic study was performed in order to understand the effects of the partial patterning on the anisotropy dependence of the ADL system. The FMR spectra as function of the applied field angle (θ_H) were obtained from micromagnetic simulations using Mumax [36]. The angular dependence was obtained at a fixed external field magnitude $H = 50$ mT, thus varying only the applied field angle, θ_H, relative to the ADL. These spectra were obtained by performing a Fourier analysis of the time dependent out-of-plane component of the magnetization, $m_z(t)$, after applying a spatially uniform field pulse in the form of $A_0 \text{sinc}(t - t_0)$, where $A_0 = 1$ mT and $t_0 = 3$ ns.

A broad study was performed, covering the angular variation of the FMR data for $t_h = 0$, 5, 10, 15, and 20 nm. In this study, the magnetic properties, the hole size and periodicity were kept constant, whilst varying the thickness, t_h, of the magnetic material in the holes [see Fig. 1(a)]. The angular dependence of the resonance modes, in the case of $t_h = 0$, 5, 10, and 20 nm are shown in Appendix C, in Fig. 15. In summary, we observed the emergence of an edge mode in the low-frequency range at $t_h = 0$ nm, whose resonance frequency tends to increase with an increasing t_h. In addition, we observed that for $t_h = 0$ nm the first fundamental mode exhibits a fourfold dependence, which is in agreement the literature. However, when considering $t_h = 15$ nm, which is shown in Fig. 10 the resonance of the edge mode overlaps with that of the first fundamental mode and as a result, the angular dependence of the resonance frequency exhibits a combined fourfold and eightfold components. Under these conditions, we were able to qualitatively reproduce the angular dependence of mode I discussed in Fig. 7).

Note that the eightfold symmetry emerges in the lowest-frequency mode, M1. Additionally, it is also noted that the higher-frequency modes, M4 and M5 exhibit a fourfold dependence shifted by 90° with respect to one another. This is important to note as a similar trend was observed in the experimental data, when discussing the modes shown in Fig. 9. One can also note that along the main directions of the ADL ($\theta_H \sim 0^\circ$ and 90°), mode M3 crosses with the mode resulting from the adjacent continuous layer (mode M2). To replicate the variation of the exchange bias field of this sample, the

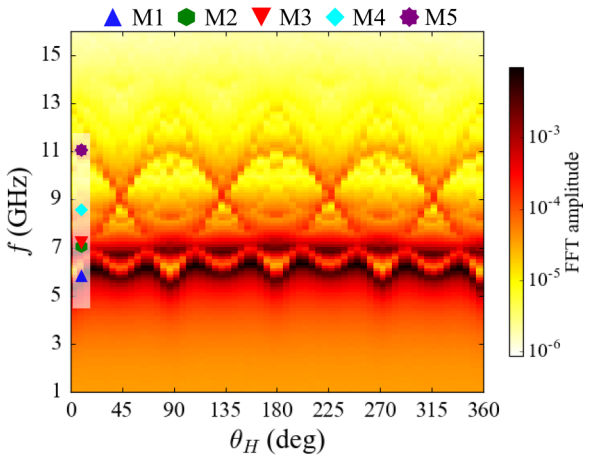

FIG. 10. Angular variation of the FMR spectra for $t_h = 15$ nm. The dark regions correspond to the resonance position. Symbols illustrate the position of the resonance modes M1–M5 at $\theta_H = 2.8^\circ$ and these can be associated with modes I, CF, II, and III obtained experimentally, while M5 may correspond to mode V of Fig. 9. Magnetic properties used in Mumax: $M_S = 1$ T, $A_{ex} = 1.3\times10^{-12}$ J/m, Landau-Lifshitz damping constant $\alpha = 0.02$ and $\theta_b = 11.25^\circ$. The discretization unit was set to 3.28 nm in the film plane and 5 nm along the direction perpendicular to the film.

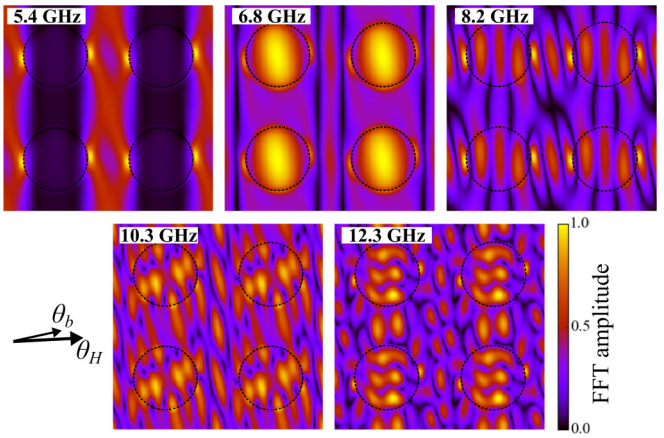

FIG. 11. Spatial distribution of the resonance modes of the ADL for $t_h = 15$ nm. The exchange bias field direction was set at $\theta_b = 11.25^\circ$. In Mumax we simulated a 2×2 array and employed boundary conditions to ensure the finite dimensions of the system did not affect the results. The size of the square unit cell was 420 nm and the hole diameter was 280 nm.

pinning field (H_b) in the micromagnetic simulations was only applied outside the holes.

To verify the superposition of the edge mode with the first fundamental mode of the ADL, we determined the spatial distribution of the resonance modes. To obtain the spatial distribution of the precession modes at fixed applied magnetic field, a time domain Fourier analysis of the magnetization component $m_z(x,y,z,t)$ was performed. In general, the precession modes in the ADL result from a localization of the precession amplitude due to the highly nonuniform demagnetisation fields and these are ultimately related to the pole distribution around the edges of the holes [20,28].

Figure 11 shows the spatial distribution of the resonance modes obtained at $\theta_H = 2.8^\circ$ with an applied field magnitude of 50 mT, while considering $t_h = 15$ nm. The normalized precession amplitude is color coded in the images and each panel appears labeled with its corresponding precession frequency. It can be noted that in the lowest-frequency mode, the mode amplitude at the edges of the holes (edge mode) overlaps with the amplitude profile corresponding to the first-order mode which extends throughout the ADL. The coupling between these two modes is maintained along all directions since the existence of the continuous layer allows the first order mode to rotate uniformly with the applied field angle. The modes at higher frequencies correspond to second- and third-order modes, given the number of amplitude nodes and the symmetry regards to the applied field angle.

We note that the amplitude of the mode corresponding to 6.8 GHz dominates in the regions of the holes (dashed circles). Nevertheless, this mode also extends through the whole lattice. Moreover, the regions with higher precession amplitude appear to be elongated along the direction perpendicular to the applied magnetic field. In the mode profiles corresponding to 8.2 and 10.3 GHz, we note that the high-amplitude regions maintain the same orientation, while in the mode corresponding to 12.3 GHz the amplitude profile appears to be elongated along the direction parallel to the applied field. Changes in the symmetry of the mode profiles are expected when considering Damon-Eshbach and backward volume modes [20,30].

The simultaneous analysis of the angular dependence of the resonance modes for $t_h = 15$ nm and the spatial distribution of the lowest resonance mode allowed us to conclude that the eightfold anisotropy in the ADL emerges due a superposition of the edge mode with the first fundamental mode. This was achieved by controlling the etch depth t_h of the ferromagnetic layer. Note that for thickness values of $t_h = 10$ nm, these two modes are separated from each other, while for $t_h = 20$ nm, the overall resonance behavior resembles a continuous exchange biased film.

V. CONCLUSIONS

We show how an exchange biased, partially etched, antidot lattice (ADL) can be used to modify the spin wave properties and introduce high-order anisotropies. Competing internal fields and modification of the exchange bias in the vicinity of the holes resulted in alterations to the ground state of the magnetic system, observed here in the form of the magnetic anisotropies with eightfold and fourfold components, which we observed from the angular dependence of four resonance modes. This feature has not been explored so far in the literature as one usually expects a fourfold component in ADL systems. The addition of the exchange bias field induces an asymmetric response of the resonance frequencies with regards to the applied field direction. These asymmetries are tunable, reaching up to 2 GHz for the lowest resonance frequency mode, and can be advantageous for microwave filtering applications. In addition, we observed that as a result of the local modifications due to structuring, the exchange bias field becomes highly dependent on the direction of the external applied field with regards to the ADL lattice, suggesting that a

stepped reversal may may be achieved by carefully controlling the lattice parameters and etch depth.

The TEM cross-sectional analysis allowed a detailed characterisation of the layer composition and the morphology of the holes. In particular, it allowed to measure the thickness of the NiFe remaining in the holes (14.5 nm). This information helped producing an accurate micromagnetic picture which in turn allowed to understand the origin of the combined eightfold and fourfold anisotropy. We have concluded that the eightfold component emerges due to an overlap between the edge mode and the first order extended mode. This may be understood from the perspective of the dipolar fields which emerge with structuring. Due to partial patterning, the dipolar interactions among the nearest holes and next-nearest holes become comparable and thus raising such anisotropic behavior. The etching of only 5 nm has ensured that the nanostructured system maintains the properties of a magnonic crystal as the spin wave dispersion (frequency versus wave vector) measured by BLS reflects the periodicity of the ADL, and the emergence of a frequency band gap of 0.6 GHz, at the edge of the first Brillouin zone.

ACKNOWLEDGMENTS

F.G. acknowledges the support by University of Glasgow and the support by the JSPS Grant-in-Aid for Scientific Research (S) (No. 25220803), the JSPS Core-to-Core Program 'A. Advanced Research Networks', and the MEXT program for promoting the enhancement of research universities (Hiroshima University). R.L.S. and G.W.P. acknowledge the support under EPSRC Grant EP/M024423/1. G.G. thanks the MIUR under PRIN Project No. 2010ECA8P3 "DyNanoMag". F.G. would like to thank Stephen Thoms, Haiping Zhou and James Grant for the enlightening discussions about nanofabrication and Sam McFadzean for the support in the TEM work.

APPENDIX A: FMR DATA OF THE CONTINUOUS FILMS

To ensure that the magnetic properties of the films have not been affected by the temperature changes throughout the fabrication process, a comparison was made between the ferromagnetic resonance data relative to the continuous film as-deposited (AD) and after the patterning process (AP). The results demonstrated that the magnetic properties have not been altered throughout the patterning process by, for example, the resist baking step. This can be seen from the comparison of the VNA-FMR data shown in Fig. 12. A summary of the fitting parameters is shown in Table II. As can be noted, the magnetic properties are identical for both AD and AP samples.

TABLE II. Fitting parameters for the continuous films at the as-deposited (AD) and post-processing (AP) stages. The residual anisotropy H_k is consistent with the value of H_k obtained in the CF mode.

Sample	H_b (T)	H_k (T)	M_{eff} (T)
AD	0.005	0.001	1.16
AP	0.0052	0.0011	1.21

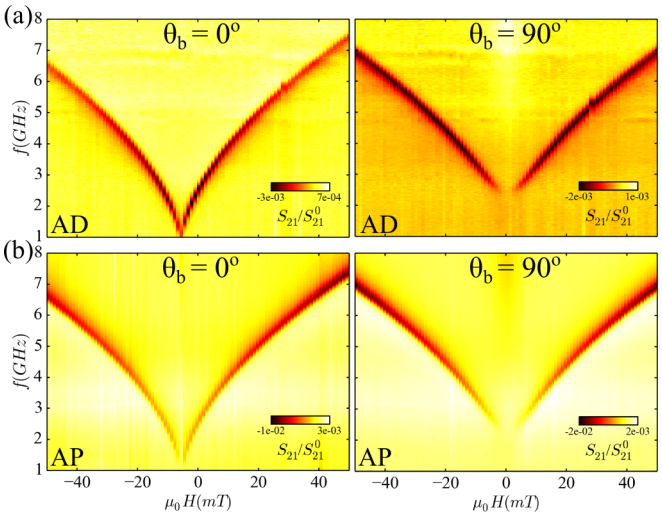

FIG. 12. FMR data from the continuous films (a) as-deposited (AD) and (b) after patterning (AP). The applied field was varied from the directions parallel ($\theta_b = 0^\circ$) and perpendicular ($\theta_b = 90^\circ$) to the exchange bias direction. The spectra in (b) were measured from a sample of continuous film which was subject to the same lithography process of the ADL, but not etched, as it was protected by the hard mask. Note that the FMR data corresponding to $\theta_b = 90^\circ$ exhibits a small exchange bias indicating that the $\mu_0 H \perp H_b$ condition was not fully satisfied.

The anisotropy field amplitude, H_k, obtained from the fitting is small on both AD and AP films so the anisotropy can be assumed negligible.

APPENDIX B: EXAMPLE OF THE FITTING OF THE EXPERIMENTAL DATA

Figure 13 corresponds to an example the multipeak fitting procedure. The derivative of the experimental data shown in Fig. 13(a) is fitted with four Lorentzian functions. All functions are fit simultaneously and across the whole field range. As we consider only the field region where the specimen is saturated, the fitted functions are also set to satisfy Kittel's resonance equation. The initial conditions necessary for the fitting are the estimates of the parameters for the Kittel equation (M_{eff}, H_a, and H_b) for each of the resonances and from there we obtain an estimate for the resonance peaks

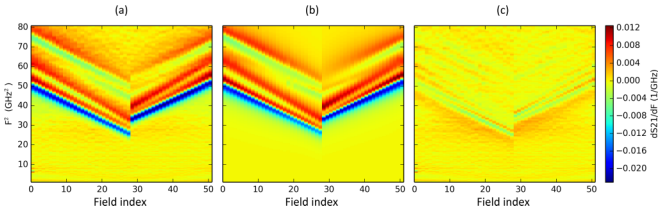

FIG. 13. (a) Derivative of the experimental data as a function of frequency and magnetic field (sweep index) corresponding to the range 60 mT $< |\mu_0 H| >$ 35 mT. (b) Plot containing the four Lorentzian shaped functions (derivative) used to fit the experimental data. (c) Plot of the residuals, which demonstrates the quality of the fit.

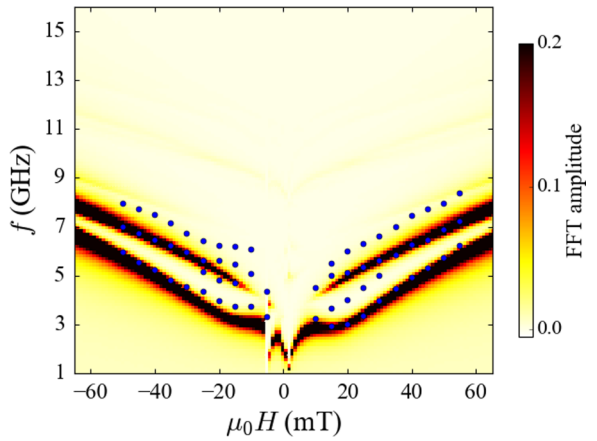

FIG. 14. Simulated FMR data (colour plot) compared with BLS data (blue markers). Magnetic properties used in the micromagnetic simulations: $M_S = 1$ T, $A_{ex} = 1.3\times10^{-12}$ J/m and $\alpha = 0.02$ and $\theta_b = 11^\circ$. The agreement at high magnetic fields suggests that the simulations conditions (magnetic properties and the geometry of the ADL) adequately reproduce the experimental data.

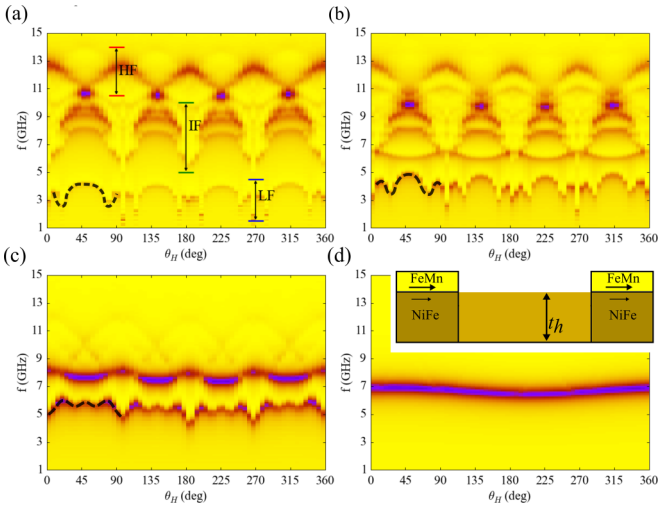

FIG. 15. (a)–(d) Angular variation of the resonance modes of the ADL for $t_h = 0$, 5, 10, and 20 nm. The exchange bias field direction was kept fixed at $\theta_b = 11.25^\circ$. Using Mumax, we simulated a 2×2 array and applied boundary conditions to ensure the finite dimensions of the system do not affect the results.

and linewidths. This set of initial conditions is then fit to the experimental data. An example of the fit is shown in Fig. 13(b). From the residual plot shown in Fig. 13(c), we note a good agreement between the experimental data and the fitted functions.

APPENDIX C: CASE STUDY

Figure 14 demonstrates the agreement between the BLS data (blue markers) and the simulated FMR spectra, suggesting that the ground state for the micromagnetic simulations has been successfully determined. In particular, note the agreement in the three lowest-frequency resonance modes and the softening of the lowest mode, at around $\mu_0 H = 20$ mT. The disagreement in the low-field region is causes by the existence of imperfections at the hole edges of the ADL, which were not recreated in micromagnetic simulations. Such imperfections will affect the reversal of the magnetization via local pinning of domains.

Figure 15 shows the calculated resonance frequency as a function of the angle, θ_H, between the applied field and the edge of the ADL. From Figs. 15(a) to 15(d), the thickness of the material in the region of the holes is set to $t_h = 0$, 5, 10 and 20 nm, respectively. For $t_h = 0$ nm we recreate a fully etched ADL and the limiting case of $t_h = 20$ nm all resonances merge in a single mode, resembling the FMR response of the mode CF discussed in the Fig. 8.

In Fig. 15(a), the high-frequency resonance band appears labeled as HF (11–14 GHz), the intermediate frequencies as IF (5.0–11 GHz) and the lowest frequency band as LF (1.5–4.8 GHz). When comparing the results of the Figs. 15(a)–15(d), we observed the following: (1) the modes in the HF band become weaker in amplitude with the increase in t_h; (2) the frequency range of the IF band becomes narrower, the amplitude of the modes become dominant and the band itself appears to shift downwards in frequency, with increasing t_h; (3) for $t_h = 0$ nm, the resonance mode in the LF band appears in the frequency range of 2–4 GHz, when $t_h = 5$ nm, the IF band appears between 3–5 GHz and in the case of $t_h = 10$ nm the LF band shifts to a range of 5–6 GHz. Importantly, we note that the angular dependence of the LF band (dashed lines) evolves to an eightfold symmetry, as t_h increases. The gradual increase in frequency of the IF band (edge mode) can be seen as direct evidence that the choice of the thickness $t_h = 15$ nm allows for an overlap between the first fundamental mode and the edge mode of the ADL lattice. In the limit shown in Fig. 15(a), for $t_h = 20$ nm, we observed that the resonance behavior equivalent to a continuous exchange biased film.

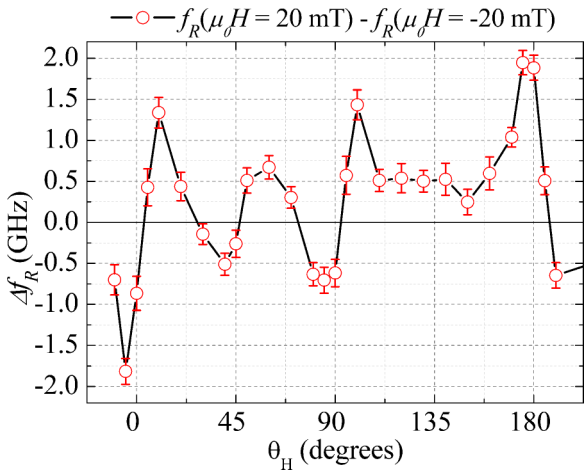

FIG. 16. Difference in resonance frequency (Δf_R) between $\mu_0 H = 20$ and -20 mT of mode I, plotted as a function of applied field angle. An asymmetry of 2 GHz can be obtained by a 10° rotation of the applied field. The oscillatory behavior of the quantity Δf_R was not obtained for $\theta_H = \sim[112.5^\circ$–$135^\circ]$, possibly due to nonuniform reversal behavior of the magnetization.

APPENDIX D: ASYMMETRY

In Sec. III C of the manuscript, the anisotropic and biased magneto-dynamic response of the ADL was discussed. It was noted that only the $H_b(\theta_H)$ of mode CF follows the $\cos(\theta_H)$ behavior of Eq. (4), which is normally obtained in continuous exchange biased films. The modes I, II, and II exhibit an oscillatory behavior different to $cos(\theta_H)$. In mode I, the oscillation of $H_b(\theta_H)$ is more pronounced, with the largest exchange bias field amplitude obtained at $\theta_H = -10^\circ$, 10°, 80°, and 100°, where $\Delta Hb \approx \pm 2$ mT (Fig. 8). At $\theta_H = 0^\circ$, the effect of the exchange bias field is not observable mainly because the spin configuration is dominated by the anisotropy of the ADL. By combining the anisotropy of the ADL and the exchange bias, one adds a degree of tuning to the resonance frequencies, whereby positive and negative frequency shifts are obtained by small variation in the applied field angle. Although the mechanism is not fully understood, the change in the polarity of the bias field may be associated with the magnetic domain texture which forms during magnetization reversal [24].

Figure 16 shows the difference (asymmetry), Δf_R, in resonance frequency between $\mu_0 H \sim 20$ and $\sin -20$ mT, as function of θ_H (consistent with Fig. 4). The applied field $|\mu_0 H| = 20$ mT represents a good approximation to the magnitude at which the softening of mode I occurs. The magnetic configuration at this applied field will be highly nonlinear at certain angles due to the proximity to the hard axis of the ADL, for example, at $\theta_H = \pm 10^\circ$. Given the eightfold oscillation in the asymmetry of Δf_R, we can confirm that the asymmetry is caused by the competition between ADL anisotropy and the exchange bias field. The asymmetry appears to have different behavior in the angle range $\theta_H =\sim [112.5^\circ$–$135^\circ]$, possibly due to nonuniform reversal behavior of the magnetization, caused by pinning near the edges of the holes, which may give rise to complex domain structures. The micromagnetic simulation results shown in Fig. 15 do not exhibit this change in polarity, as can be understood by comparing the spectra at $\theta_H = 10^\circ$ and $\theta_H = 350^\circ$, suggesting that by simply defining the exchange bias as a pinning field may be an incomplete approach to the problem of exchange bias in patterned structures. Local deformations of the magnetic domain texture imposed by the patterning of the holes or roughness at the interface between the $Ni_{80}Fe_{20}$ and $Fe_{50}Mn_{50}$ films may also occur, allowing for nonuniform magnetization reversal.

[1] M. Krawczyk and D. Grundler, Review and prospects of magnonic crystals and devices with reprogrammable band structure, J. Phys.: Condens. Matter **26**, 123202 (2014).

[2] B. Lenk, H. Ulrichs, F. Garbs, and M. Munzenberg, The building blocks of magnonics, Phys. Rep. **507**, 107 (2011).

[3] E. K. Semenova and D. V. Berkov, Spin wave propagation through an antidot lattice and a concept of a tunable magnonic filter, J. Appl. Phys. **114**, 013905 (2013).

[4] R. Morales, M. Kovylina, I. K. Schuller, A. Labarta, and X. Batlle, Antiferromagnetic/Ferromagnetic nanostructures for multidigit storage units, Appl. Phys. Lett. **104**, 032401 (2014).

[5] C. Yu, M. J. Pechan, and G. J. Mankey, Dipolar induced, spatially localized resonance in magnetic antidot arrays, Appl. Phys. Lett. **83**, 3948 (2003).

[6] S. Tacchi, M. Madami, G. Gubbiotti, G. Carlotti, A. O. Adeyeye, S. Neusser, B. Botters, and D. Grundler, Angular dependence of magnetic normal modes in NiFe antidot lattices with different lattice symmetry, IEEE Trans. Magn. **46**, 1440 (2010).

[7] G. Duerr, S. Tacchi, G. Gubbiotti, and D. Grundler, Field-controlled rotation of spin-wave nanochannels in bi-component magnonic crystals, J. Phys. D **47**, 325001 (2014).

[8] J. Ding and A. O. Adeyeye, Binary ferromagnetic nanostructures: Fabrication, static and dynamic properties, Adv. Funct. Mater. **23**, 1684 (2013).

[9] X. M. Liu, J. Ding, and A. O. Adeyeye, Magnetization dynamics and reversal mechanism of Fe filled $Ni_{80}Fe_{20}$ antidot nanostructures, Appl. Phys. Lett. **100**, 242411 (2012).

[10] G. Gubbiotti, P. Malagò, S. Fin, S. Tacchi, L. Giovannini, D. Bisero, M. Madami, G. Carlotti, J. Ding, A. O. Adeyeye, and R. Zivieri, Magnetic normal modes of bicomponent permalloy/cobalt structures in the parallel and antiparallel ground state, Phys. Rev. B **90**, 024419 (2014).

[11] M. Kovylina, M. Erekhinsky, R. Morales, J. E. Villegas, I. K. Schuller, A. Labarta, and X. Batlle, Tuning exchange Bias in Ni/FeF_2 heterostructures using antidot arrays, Appl. Phys. Lett. **95**, 152507 (2009).

[12] W. Zhang, D. N. Weiss, and K. M. Krishnan, Competing anisotropies and temperature dependence of exchange bias in CoFeIrMn metallic wire arrays fabricated by nanoimprint lithography, J. Appl. Phys. **107**, 09D724 (2010).

[13] F. J. T. Goncalves, R. D. Desautels, S. Su, T. Drysdale, J. van Lierop, K.-W. Lin, D. S. Schmool, and R. L. Stamps, Anisotropy engineering using exchange bias on antidot templates, AIP Adv. **5**, 067101 (2015).

[14] G. Duerr, M. Madami, S. Neusser, S. Tacchi, G. Gubbiotti, G. Carlotti, and D. Grundler, Spatial control of spin-wave modes in $Ni_{80}Fe_{20}$ antidot lattices by embedded Co nanodisks, Appl. Phys. Lett. **99**, 202502 (2011).

[15] J. Nogues and I. K. Schuller, Exchange bias, J. Magn. Magn. Mater. **192**, 203 (1999).

[16] R. L. Stamps, Mechanisms for exchange bias, J. Phys. D **34**, 444 (2001).

[17] K. Liu, S. Baker, M. Tuominen, T. Russell, and I. Schuller, Tailoring exchange bias with magnetic nanostructures, Phys. Rev. B **63**, 060403 (2001).

[18] M. T. Rahman, N. N. Shams, D. S. Wang, and C.-H. Lai, Enhanced exchange Bias in sub-50-nm IrMn/CoFe nanostructure, Appl. Phys. Lett. **94**, 082503 (2009).

[19] S. Neusser, B. Botters, M. Becherer, D. Schmitt-Landsiedel, and D. Grundler, Spin-wave localization between nearest and next-nearest neighboring holes in an antidot lattice, Appl. Phys. Lett. **93**, 122501 (2008).

[20] S. Neusser, B. Botters, and D. Grundler, Localization, confinement, and field-controlled propagation of spin waves in $Ni_{80}Fe_{20}$ antidot lattices, Phys. Rev. B **78**, 054406 (2008).

[21] S. Tacchi, M. Madami, G. Gubbiotti, G. Carlotti, A. O. Adeyeye, S. Neusser, B. Botters, and D. Grundler, Magnetic normal modes in squared antidot array with circular holes: A combined Brillouin light scattering and broadband ferromagnetic resonance study, IEEE Trans. Magn. **46**, 172 (2010).

[22] S. Neusser, G. Duerr, S. Tacchi, M. Madami, M. L. Sokolovskyy, G. Gubbiotti, M. Krawczyk, and D. Grundler, Magnonic minibands in antidot lattices with large spin-wave propagation velocities, Phys. Rev. B **84**, 094454 (2011).

[23] J. Sklenar, V. S. Bhat, L. E. DeLong, O. Heinonen, and J. B. Ketterson, Strongly localized magnetization modes in permalloy antidot lattices, Appl. Phys. Lett. **102**, 152412 (2013).

[24] V. Bhat, J. Woods, L. E. De Long, J. T. Hastings, J. Sklenar, J. B. Ketterson, and M. Pechan, FMR study of permalloy films patterned into square lattices of diamond antidots, IEEE Trans. Magn. **49**, 1029 (2013).

[25] X. Kong, D. Krasa, H. P. Zhou, W. Williams, S. McVitie, J. M. R. Weaver, and C. D. W. Wilkinson, Very high resolution etching of magnetic nanostructures in organic gases, Microelectron. Eng. **85**, 988 (2008).

[26] G. Carlotti and G. Gubbiotti, Magnetic properties of layered nanostructures studied by means of Brillouin light scattering and the surface magneto-optical Kerr effect, J. Phys.: Condens. Matter **14**, 8199 (2002).

[27] R. Zivieri, P. Malagò, L. Giovannini, S. Tacchi, G. Gubbiotti, and A. O. Adeyeye, Soft magnonic modes in two-dimensional permalloy antidot lattices, J. Phys.: Condens. Matter **25**, 336002 (2013).

[28] R. Zivieri, S. Tacchi, F. Montoncello, L. Giovannini, F. Nizzoli, M. Madami, G. Gubbiotti, G. Carlotti, S. Neusser, G. Duerr, and D. Grundler, Bragg diffraction of spin waves from a two-dimensional antidot lattice, Phys. Rev. B **85**, 012403 (2012).

[29] S. Tacchi, G. Duerr, J. W. Klos, M. Madami, S. Neusser, G. Gubbiotti, G. Carlotti, M. Krawczyk, and D. Grundler, Forbidden Band Gaps in the Spin-Wave Spectrum of a Two-Dimensional Bicomponent Magnonic Crystal, Phys. Rev. Lett. **109**, 137202 (2012).

[30] J. Sklenar, V. S. Bhat, C. C. Tsai, L. E. DeLong, and J. B. Ketterson, Generating wave vector specific Damon-Eshbach spin waves in Py using a diffraction grating, Appl. Phys. Lett. **101**, 052404 (2012).

[31] E. Mengotti, L. J. Heyderman, F. Nolting, B. R. Craig, J. N. Chapman, L. Lopez-Diaz, R. J. Matelon, U. G. Volkmann, M. Klaui, U. Rudiger, C. A. F. Vaz, and J. A. C. Bland, Easy axis magnetization reversal in cobalt antidot arrays, J. Appl. Phys. **103**, 5 (2008).

[32] N. G. Deshpande, M. S. Seo, S. J. Lee, L. Y. Chen, K. W. Kim, J. Y. Rhee, Y. H. Kim, and Y. P. Lee, Magnetization reversal mechanism of bilayered magnetic anti-dot lattices, J. Appl. Phys. **111**, 013906 (2012).

[33] F. Haering, U. Wiedwald, S. Nothelfer, B. Koslowski, P. Ziemann, L. Lechner, A. Wallucks, K. Lebecki, U. Nowak, J. Gräfe, E. Goering, and G. Schütz, Switching modes in easy and hard axis magnetic reversal in a self-assembled antidot array, Nanotechnology **24**, 465709 (2013).

[34] C. Kittel, On the theory of ferromagnetic resonance absorption, Phys. Rev. **73**, 155 (1948).

[35] J. Nogues, J. Sort, V. Langlais, V. Skumryev, S. Surinach, J. S. Munoz, and M. D. Baro, Exchange bias in nanostructures, Phys. Rep. **422**, 65 (2005).

[36] A. Vansteenkiste, J. Leliaert, M. Dvornik, M. Helsen, F. Garcia-Sanchez, and B. V. Waeyenberge, The design and verification of MuMax3, AIP Adv. **4**, 107133 (2014).